Simulation of high-viscosity-ratio multicomponent fluid flow using a pseudopotential model based on the nonorthogonal central-moments lattice Boltzmann method

Farshad Gharibi[*] and Mahmud Ashrafizaadeh[†]
Department of Mechanical Engineering, Isfahan University of Technology, Isfahan 84156, Iran

(Received 14 December 2019; accepted 29 March 2020; published 28 April 2020)

In this research, the development of a pseudopotential multicomponent model with the capability of simulating high-viscosity-ratio flows is discussed and examined. The proposed method is developed based on the nonorthogonal central moments model in the lattice Boltzmann method, and the exact difference model (EDM) is used to apply the intercomponent interaction force. In contrast to the original Shan-Chen model, in which the applying force has the viscosity-dependent error term, the error term of this model does not depend on the viscosity. A GPU parallel CUDA code has been developed and is employed to study the proposed method. Different cases are considered to evaluate the ability of the model, including the Laplace test, a static droplet, and a two-component concurrent channel flow. Also, wetting and nonwetting relative permeabilities for flows with dynamic viscosity ratios between 0.0002 and 5000 are predicted. Numerical results are compared with those of available analytical solutions. Very good agreement between these results are observed. The model has the capability of simulating multicomponent flows with very low kinematic viscosities of the order of 10^{-5} and dynamic viscosity ratios of up to an order of 10^4, which is a much wider range compared with that of existing pseudopotential models. Furthermore, the results showed that the parallel processing on GPU significantly accelerated computations. The present parallel performance evaluation shows that the CUDA parallel can achieve about 41 times improvement than the CPU serial implementation. The aforementioned enhancement increases the flexibility of the multicomponent lattice Boltzmann method and its applicability to a broader spectrum of engineering applications.

DOI: 10.1103/PhysRevE.101.043311

I. INTRODUCTION

Multicomponent fluid flows occur in many engineering and industrial applications. Hence, their simulation is of high interest to many researchers [1]. Due to the wide variety of fluid properties, the capability of numerical models to apply appropriate thermo-physical properties for the simulation of engineering problems is also very important [1,2]. The stability and accuracy of a multicomponent method for the simulation of flows with a wide range of viscosity ratios is an especially important capability for realistic applications such as flows through rocks [2], underground water and oil flows, and many other engineering and industrial situations.

In recent years, among the methods of computational fluid dynamics, the lattice Boltzmann method (LBM) has been very much considered due to its inherent properties such as the particle-like nature, the easy application of boundary conditions in complex geometries, and the simple algorithm [3,4]. Also, this method is highly parallelizable so that, this particular feature has been a motive to parallelize the LBM using GPUs, see, e.g., [5–7].

One of the most popular models for multicomponent fluid flow simulations in the LBM is the pseudopotential model [8]. The pseudopotential method is used to simulate a variety of problems, such as multicomponent turbulence flows [9], multicomponent fluid flows in porous media [10–13], multicomponent particulate fluid flows [14,15], and many other problems. However, this method has some limitations, such as the existence of spurious currents at the interface [16–18], and the numerical instability in the large viscosity ratio multicomponent fluid flow simulations [19,20]. These limitations have shown up in research conducted by previous researchers. For example, Ghassemi and Pak [11] have studied the relative permeability of two immiscible fluids flowing in porous media using the original pseudopotential method. In their research, the simulation was performed up to a viscosity ratio of three due to the limitation of the pseudopotential method. Yang and Boek [21] stated in their study that the results of the two-component Poiseuille flow simulation with the pseudopotential method, in the viscosity ratio of 10 are not accurate and there is some noise in the vicinity of the interface. Berghout and Van den Akker [22] investigated the droplet formation at an aperture by using the pseudopotential method. In their research, they stated that, because of the limitations of the method, they used the equivalent viscosity assumption for both fluids, which is an enormous simplification.

In recent years, several scientific efforts have been made to improve the performance of the pseudopotential multiphase and multicomponent models. Some researchers tried to reduce the spurious current by making sufficient spatial isotropy in the calculation of intercomponent interaction,

[*]f.gharibi@me.iut.ac.ir
[†]mahmud@cc.iut.ac.ir

see, e.g., Refs. [16–18]. Other studies have been focused on the improvement of the force method in the pseudopotential model. In the multiphase and multicomponent pseudopotential method provided by Shan and Chen, they proposed the shifting velocity method for applying interphase force [23]. This force model has an error term that depends on the fluid's viscosity [24]. Other models have also been used to apply the interphase interaction force in the pseudopotential method. Kupershtokh *et al.* [25] used the exact difference method in the two-phase pseudopotential model. They showed by using this force model, to apply the interphase interaction force, the dependency of the phase density on the viscosity that exists in the original pseudopotential model disappears, and the stability of the model increases. In the EDM model, the error term is not dependent on the viscosity [24]. Li *et al.* [26] evaluated a modified force model, based on Gou's force model [27], in their two-phase pseudopotential method.

On the other hand, one of the limitations in applying the low viscosity and simulating a high viscosity ratio flow is the instability of LBM collision models. Some researchers have tried to improve the multicomponent pseudopotential method by using a more stable collision method. Porter *et al.* [1] used the multiple relaxation time (MRT) collision model combined with the explicit force (EF) scheme to achieve a dynamic viscosity ratio of up to 1000 and the lowest kinematic viscosity of 0.0067 lattice units. Otomo *et al.* [2] achieved a dynamic viscosity ratio of 1000 and a minimum kinematic viscosity of 0.0017 by using the regularized collision model.

Geier *et al.* [28] presented a collision model based on central moments that satisfies a higher degree of Galilean invariants associated with the collision operator in the LBM. Recently, De Rosis [29] presented a collision model based on the nonorthogonal sets of central moments. This model has the same stability as the orthogonal central moments models, but the complexity of equations is greatly reduced, and implementation of the method is easy.

This study aims to provide a computationally stable and accurate method for simulating high-viscosity-ratio multicomponent fluid flows by studying the capabilities of the nonorthogonal central moment collision model for multicomponent fluid flow simulation by using the pseudopotential model. In this research, it is attempted by developing the pseudopotential model based on the non-orthogonal central moments model and using the advantages of the EDM force scheme to present a model for simulating high-viscosity-ratio multicomponent fluid flows. A CUDA computational code is developed and implemented in the present simulations, and the capabilities of this model are investigated.

II. NUMERICAL METHOD

A. Nonorthogonal central moment lattice Boltzmann method

The LBM is a mesoscopic model proposed by McNamara and Zanetti in 1988 [30]. This method is based on the calculation of the distribution function for particles that move and collide on a lattice. The lattice Boltzmann equation with a force term can be expressed as [31]

$$f_i(\mathbf{x}+\mathbf{e}_i\delta t,\ t+\delta t) = f_i(\mathbf{x},t) + \Omega_i + F_i, \tag{1}$$

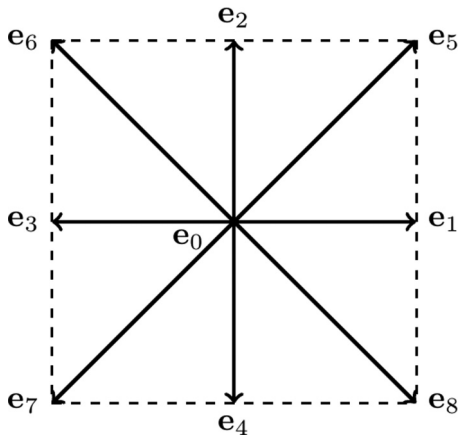

FIG. 1. D2Q9 model.

where f_i is the distribution function for different lattice directions, $\mathbf{e}_i = [e_{x_i}, e_{y_i}]$ is the discrete particle velocity, and $\mathbf{x}$ and t represent the location of the fluid nodes and time, respectively. Ω is the collision operator and F is an external force. The right side of the equation shows the effect of particle collisions and external forces on the change in the distribution function. Equation (1) can be written in two steps, including collision and streaming, to simplify the numerical algorithm [32]:

collision:

$$f_i^{\star}(\mathbf{x},t+\delta t) = f_i(\mathbf{x},t) + \Omega_i + F_i, \tag{2}$$

streaming:

$$f_i(\mathbf{x}+\mathbf{e}_i\delta t,\ t+\delta t) = f_i^{\star}(\mathbf{x},t+\delta t), \tag{3}$$

where $f_i^{\star}$ is the postcollision distribution function. In the present study, the D2Q9 model is used to simulate two-dimensional fluid flow. According to Fig. 1, the D2Q9 model has nine discrete particle velocities that take the following values:

$$\mathbf{e}_i = \begin{cases} (0,0) & i:0 \\ (1,0)(0,1)(-1,0)(0,-1) & i:1,2,3,4 \\ (1,1)(-1,1)(-1,-1)(1,-1) & i:5,6,7,8. \end{cases} \tag{4}$$

The macroscopic density (ρ) and velocity ($\mathbf{U}$) will be obtained from the following equations:

$$\rho(\mathbf{x},t) = \sum_{i=0}^{8} f_i(\mathbf{x},t), \tag{5}$$

$$\rho\mathbf{U}(\mathbf{x},t) = \sum_{i=0}^{8} \mathbf{e}_i f_i(\mathbf{x},t). \tag{6}$$

Now, to define the collision operator, the central moments K are obtained as [29]

$$k_{x^m y^n} = \sum_{i=0}^{8} f_i \bar{e}_{x,i}^{m} \bar{e}_{y,i}^{n}, \tag{7}$$

where $m = 0, 1, 2$ and $n = 0, 1, 2$ and $\bar{e}$ is defined as

$$\begin{aligned} \bar{e}_{x,i} &= e_{x,i} - u_x, \\ \bar{e}_{y,i} &= e_{y,i} - u_y. \end{aligned} \tag{8}$$

To perform the transformation from the distribution functions' space to the central moments' space, the transformation matrix T, according to the Ref. [29], is defined as follows:

$$T = [|\overline{T}_0\rangle, \ldots, |\overline{T}_8\rangle], \tag{9}$$

where $|\overline{T}_i\rangle$ are column vectors that are defined by

$$\begin{aligned}
|\bar{T}_0\rangle &= ||\bar{\mathbf{e}}_i|^0\rangle \\
|\bar{T}_1\rangle &= |\bar{e}_{xi}\rangle, \\
|\bar{T}_2\rangle &= |\bar{e}_{yi}\rangle, \\
|\bar{T}_3\rangle &= |\bar{e}_{xi}^2 + \bar{e}_{yi}^2\rangle, \\
|\bar{T}_4\rangle &= |\bar{e}_{xi}^2 - \bar{e}_{yi}^2\rangle, \\
|\bar{T}_5\rangle &= |\bar{e}_{xi}\bar{e}_{yi}\rangle, \\
|\bar{T}_6\rangle &= |\bar{e}_{xi}^2\bar{e}_{yi}\rangle, \\
|\bar{T}_7\rangle &= |\bar{e}_{xi}\bar{e}_{yi}^2\rangle, \\
|\bar{T}_8\rangle &= |\bar{e}_{xi}^2\bar{e}_{yi}^2\rangle.
\end{aligned} \tag{10}$$

By transforming the particle distribution functions to the moment space, central moments will be obtained as follows:

$$\begin{aligned}
k_0 &= \rho, \\
k_1 &= k_x, \\
k_2 &= k_y, \\
k_3 &= k_{xx} + k_{yy}, \\
k_4 &= k_{xx} - k_{yy}, \\
k_5 &= k_{xy}, \\
k_6 &= k_{xxy}, \\
k_7 &= k_{xyy}, \\
k_8 &= k_{xxyy}.
\end{aligned} \tag{11}$$

Also, the equilibrium central moments k^{eq} are obtained by replacing f_i with f_i^{eq} through Eqs. (7) and (11). Based on the order-three expansion of the Maxwell equilibrium distribution function, the discrete equilibrium distribution function can be obtained from the following equation [33,34]:

$$\begin{aligned}
f_i^{eq}(\mathbf{x}, t) = w_i\rho\Bigg[1 + \frac{\mathbf{e}_i \cdot \mathbf{U}}{c_s^2} + \frac{(\mathbf{e}_i \cdot \mathbf{U})^2}{2c_s^4} - \frac{(\mathbf{U})^2}{2c_s^2} \\
+ \frac{(\mathbf{e}_i \cdot \mathbf{U})^3}{6c_s^6} - \frac{\mathbf{e}_i \cdot \mathbf{U}}{2c_s^4}\mathbf{U}^2\Bigg],
\end{aligned} \tag{12}$$

where w_i is the weight factor of the D2Q9 lattice model, and c_s is the lattice speed of sound. Now, the postcollision central moments $k_i^\star$ can be calculated by

$$k_i^\star = k_i + \omega_i\big(k_i^{eq} - k_i\big), \tag{13}$$

where ω_i is the relaxation frequency related to k_i. Only the ω_4 and ω_5 relaxation frequencies are related to the fluid's kinematic viscosity ν according to the following equations:

$$\omega_{4,5} = \frac{1}{\tau}, \tag{14}$$

$$\nu = (\tau - 0.5)c_s^2, \tag{15}$$

where τ is the relaxation time. The ω_3 frequency is related to the bulk viscosity, and the other frequencies are related to the higher-order moments. In this study, all frequencies except ω_4 and ω_5 are considered equal to one according to Ref. [29].

Now, by multiplying the inverse of the transformation matrix with the postcollision moments, the postcollision distribution functions can be obtained. To apply the external force, the EDM model can be used. This force model is extracted directly from the Boltzmann equation and is not dependent on the collision model. Hence, the EDM model can be used in each collision model [25]. Therefore, the postcollision distribution functions with the external force term can be obtained through the relation presented in Eq. (A1).

B. Multicomponent pseudopotential method

The multicomponent pseudopotential method was proposed by Shan and Chen in 1993 [23]. This method works based on the interparticle attraction and repulsion forces in the LBM. In the Shan-Chen multicomponent model, the LBM equation can be written as

$$f_i^\sigma(\mathbf{x} + \mathbf{e}_i\delta t,\ t + \delta t) = f_i^\sigma(\mathbf{x}, t) + \Omega_i^\sigma + F_i^\sigma. \tag{16}$$

In this equation, σ is a components counter. If the lattice Boltzmann equation with the central moments collision operator is rewritten in the matrix form, then this will be

$$\begin{aligned}
&f_i^\sigma(\mathbf{x} + \mathbf{e}_i\delta t,\ t + \delta t) - f_i^\sigma(\mathbf{x}, t) \\
&\quad = T^{-1}S^\sigma T\left(f_i^{eq,\sigma}(\mathbf{x}, t) - f_i^\sigma(\mathbf{x}, t)\right) + F_i^\sigma.
\end{aligned} \tag{17}$$

In this equation, $f_i^{eq,\sigma}$, in accordance with the pseudopotential method, is obtained from Eq. (12), by using the effective velocity ($\mathbf{U}^{eq}$). According to Refs. [28,29] the central moments, moments displaced by the velocity, in the multicomponent model is defined as displaced moments by the effective velocity $\mathbf{U}^{eq}$. So, by replacing f_i with $f_i^{eq,\sigma}$ through Eqs. (7) and (11) and several algebraic manipulations the following expressions for equilibrium central moments can be obtained:

$$\begin{aligned}
k_0^{eq,\sigma} &= \rho^\sigma, \\
k_1^{eq,\sigma} &= k_2^{eq,\sigma} = k_4^{eq,\sigma} = k_5^{eq,\sigma} = k_6^{eq,\sigma} = k_7^{eq,\sigma} = 0, \\
k_3^{eq,\sigma} &= (2/3)\rho^\sigma, \\
k_8^{eq,\sigma} &= (1/9)\rho^\sigma - \rho^\sigma(\mathbf{U}^{eq})^2.
\end{aligned} \tag{18}$$

As can be seen from Eq. (18), with the usage of these central moments, all operations except $k_8^{eq,\sigma} = k_{xxyy}$ are independent of the choice of the coordinate system. In Eq. (17), S^σ is the diagonal matrix of the relaxation frequencies and is defined as

$$S^\sigma = \mathrm{diag}\big[\omega_0^\sigma,\ \omega_1^\sigma,\ \omega_2^\sigma,\ \omega_3^\sigma,\ \omega_4^\sigma,\ \omega_5^\sigma,\ \omega_6^\sigma,\ \omega_7^\sigma,\ \omega_8^\sigma\big]. \tag{19}$$

The following equation is used to calculate the intercomponent force F_{int} in the Shan-Chen model:

$$F_{\mathrm{int}}^\sigma(\mathbf{x}, t) = -G\psi^\sigma(\mathbf{x}, t)\sum_i w_i\psi^{\sigma'}(\mathbf{x} + \mathbf{e}_i\delta t, t)\mathbf{e}_i, \tag{20}$$

where G is an amplifying coefficient associated with the surface tension, which by changing it, it is possible to adjust the surface tension. ψ is an effective density, which is considered equal to ρ in this study. In this research, an isotropy order of 10 is implemented to calculate the intercomponent forces

according to the Ref. [17]. To conserve momentum in the absence of external force, according to Refs. [1,23,35], the effective velocity of fluid ($\mathbf{U}^{eq}$) can be obtained as follows: Since only the ω_1 and ω_2 relaxation frequencies are related to momentum, the following equation must be satisfied for the momentum conservation:

$$\left(T\left[\sum_{\sigma} T^{-1} S^{\sigma} T\left(f_i^{eq,\sigma}(\mathbf{x},t) - f_i^{\sigma}(\mathbf{x},t)\right)\right]\right)_{1,2} = 0, \quad (21)$$

where 1 and 2 indicate the rows of the transformation matrix. Since the transformation matrix T depends only on the effective velocity, and noting that $S^{\sigma}_{1,2} = \omega^{\sigma}_{1,2}$, the previous equation is simplified to

$$\left(\sum_{\sigma} \omega_j^{\sigma} \sum_i \bar{\mathbf{e}}_i\left(f_i^{eq,\sigma}(\mathbf{x},t) - f_i^{\sigma}(\mathbf{x},t)\right) = 0\right)_{j=1,2} = 0. \quad (22)$$

Given that, in this study, $\omega^{\sigma}_{1,2}$ are considered to be 1, after simplification, the effective velocity will be obtained as follows:

$$\mathbf{U}^{eq} = \frac{\sum_{\sigma} \rho^{\sigma} \mathbf{U}^{\sigma}}{\sum_{\sigma} \rho^{\sigma}}. \quad (23)$$

To apply the surface-wetting condition, the fluid-solid adhesive force F_s in the vicinity of the solid is obtained through [36]

$$F_s^{\sigma}(\mathbf{x},t) = -G_s^{\sigma} \psi^{\sigma}(\mathbf{x},t) \sum_i \omega_i S'(\mathbf{x} + \mathbf{e}_i \delta t,\ t)\mathbf{e}_i, \quad (24)$$

where S' is considered equal to one for solid lattices and equal to zero for fluid lattices, and G_s^{σ} controls the strength of the fluid-solid adhesive force. For a two-component system, usually $G_s^1 = -G_s^2$. The total force F_{tot} is obtained by the summation of all volume forces. In the EDM model, the effect of the total force is considered as a change in the equilibrium distribution function. In this model, presented by Kopershtokh *et al.* [25], a force term is added to the Boltzmann equation by the following equation:

$$F_i^{\sigma} = f_i^{eq,\sigma}\left(\rho^{\sigma},\ \mathbf{U}^{eq} + \frac{F_{\text{tot}}^{\sigma}}{\rho^{\sigma}}\right) - f_i^{eq,\sigma}(\rho^{\sigma},\ \mathbf{U}^{eq}). \quad (25)$$

Also, the actual velocity of the fluids ($\mathbf{U}^{*\sigma}$) is calculated in half-time step, using this model:

$$\rho^{\sigma} \mathbf{U}^{*\sigma} = \sum_i \mathbf{e}_i f_i + \frac{F_{\text{tot}}^{\sigma} \Delta t}{2}, \quad (26)$$

where Δt is the time step. The actual mixture velocity is also calculated as follows:

$$\mathbf{U}^{*} = \frac{\sum_{\sigma} \rho^{\sigma} \mathbf{U}^{*\sigma}}{\sum_{\sigma} \rho^{\sigma}}. \quad (27)$$

III. RESULTS AND DISCUSSION

In this section, using the proposed model described in the previous sections, several test cases have been studied to show the abilities and accuracy of the proposed method to simulate multicomponent fluid flow. These cases include the investigation of static droplets and fluid flow in the two-dimensional (2D) channel. In the case of static droplets, several tests include: the Laplace law test, the magnitude of the spurious current, the independence of surface tension on the viscosity ratio, the highest viscosity ratio to achieve, and the hydrophobic and hydrophilic behavior of the surface have been studied. Also, in the case of the 2D channel, the velocity profile in different cases and the relative permeability prediction have been investigated. It is worth noting that all the results presented in this study are based on the lattice units.

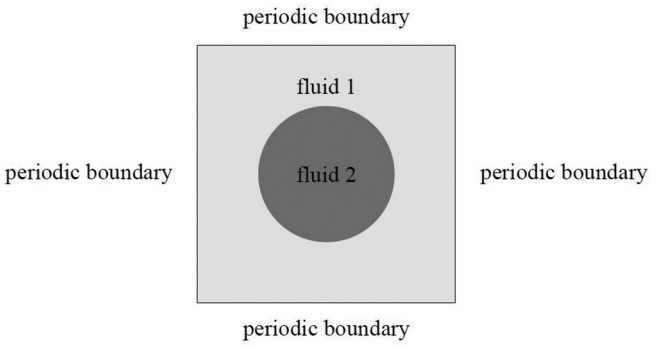

FIG. 2. A schematic view of the geometry of static droplet simulation.

A. Static droplets

In this simulation, a static circular droplet embedded in a different suspending fluid is investigated. This simulation is studied in a square domain with the periodic boundary conditions in all its sides. Figure 2 shows a schematic of this simulation. Physically, the system should be relaxed to equilibrium, and according to the Laplace law, the pressure difference between inside and outside of the droplet should be balanced by the surface tension [20]. To investigate the capability of the proposed model to simulate the high dynamic viscosity ratio, a droplet with a radius of $R = 40$ is investigated in a domain with the dimension of 254×254 and the amplitude factor of $G = 2.0$. Figure 3 shows the density of the droplet for a dynamic viscosity ratio of $M = 10^5$ after 10^4 time steps. Figure 4 shows the magnitude of

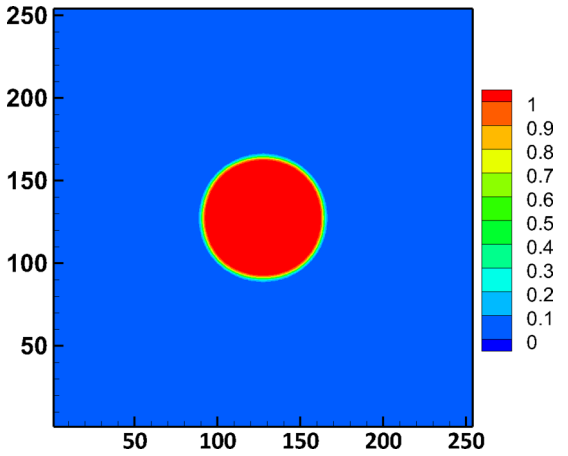

FIG. 3. The density contour of the droplet with radius of $R = 40$ and dynamic viscosity ratio $M = 10^5$.

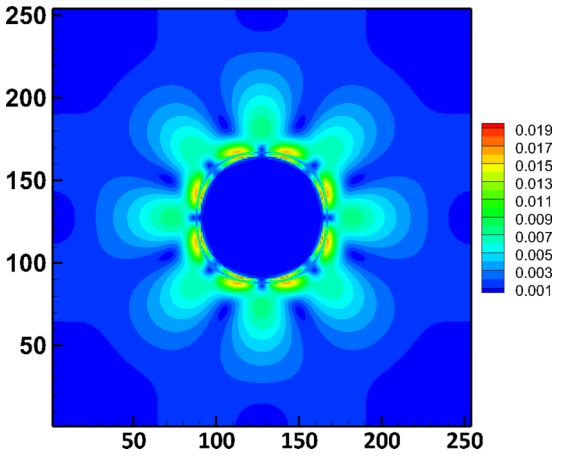

FIG. 4. The contour of spurious velocity for the droplet with the radius of $R = 40$ in the dynamic viscosity ratio of $M = 10^5$.

spurious velocity in this dynamic viscosity ratio. As the results show, the proposed model has a high capability to simulate a dynamic viscosity ratio in the order of 10^4. In this simulation, the kinematic viscosity of the surrounded fluid is set as $\nu_1 = 3.33 \times 10^{-5}$, while in the models presented in Refs. [1] and [2], the lowest fluid kinematic viscosity is $\nu_1 = 0.0067$ and $\nu_1 = 0.0017$, respectively.

To examine the Laplace law and calculate the surface tension, a domain with the dimension of 254×254 is considered. The density of both fluids in this simulation is considered to be one, and the investigations are carried out for three dynamic viscosity ratios of 1, 5000, and 0.0002. Figure 5 shows the results of this simulation for the amplifying coefficients of $G = 2$ and $G = 2.5$. By changing the coefficient G, the surface tension, which can be obtained from the slope of the line $dP - R^{-1}$, is changed and different surface tension can be obtained by adjusting G, as can be seen in Fig. 5. According to Fig. 5 it can also be seen that, contrary to the results of the original Shan-Chen model, which was reported by Dong *et al.* [37], in the presented model, the surface tension in a wide range of the dynamic viscosity ratios is not dependent to the dynamic viscosity ratio, as it should be expected.

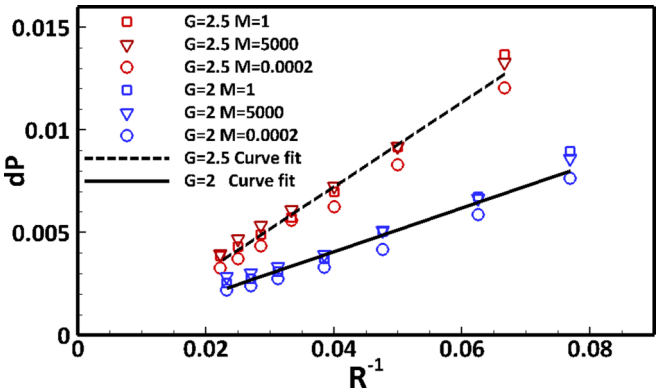

FIG. 5. The pressure difference between the inside of droplet and the surrounding fluid in terms of the inverse of the droplet radius for the surface tensions of 0.21 and 0.1.

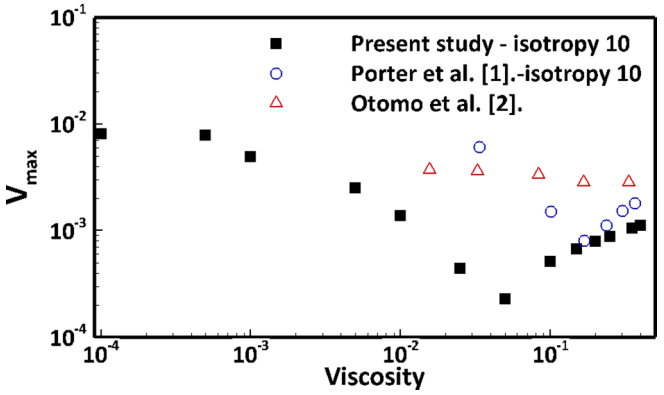

FIG. 6. Maximum spurious velocity magnitude for different viscosities in the dynamic viscosity ratio of $M = 1$.

To determine the magnitude of the spurious velocity and the dependence of the spurious velocity on the viscosity of the fluids, a droplet with a radius of 24 in a domain with 62×62 lattice nodes is investigated. The dynamic viscosity ratio in this simulation is set as 1 and the surface tension is set as 0.075 (lattice units). The maximum spurious velocity resulting from the simulation for different kinematic viscosity in the range of 0.0001 to 0.35 is investigated. Figure 6 shows the maximum spurious velocity in terms of kinematic viscosity in this simulation. In this figure, the results are compared with the results presented by Refs. [1] and [2]. Figure 7 shows the magnitude of the spurious velocity for the different dynamic viscosity ratio for a droplet with a radius of 24 and the surface tension of 0.075 (lattice units) in a 62×62 lattice domain. As can be seen, the spurious velocities in this model are less than the previous models at dynamic viscosity ratios less than 300 but, unfortunately, with increasing dynamic viscosity ratio, an increase in the magnitude of the spurious velocities is observable for isotropy order of 10.

Furthermore, the capability of the model to produce different contact angles is studied. The simulation is investigated in a 256×128 domain, with the upper and lower boundaries solid, and the right and left boundaries periodic. A semicircular droplet of a component is placed on the bottom wall, and simulations for different G_s values are investigated. The results of this simulation, shown in Fig. 8, show tha,t by adjusting G_s, different contact angles can be achieved.

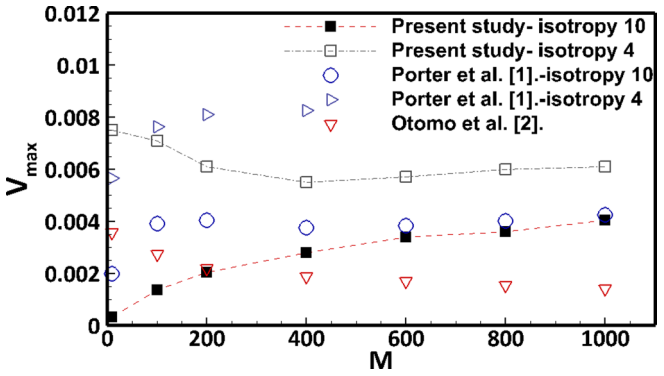

FIG. 7. Maximum spurious velocity for different dynamic viscosity ratios (kinematic viscosity of surrounding fluid is 0.0067).

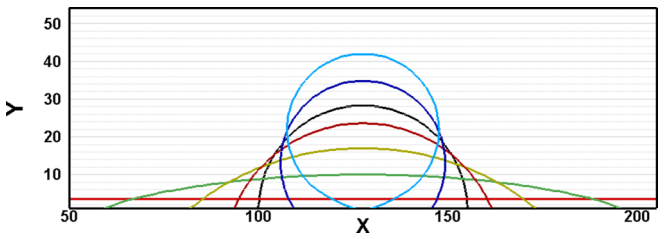

FIG. 8. Interface shape of droplet for different contact angles for $G_s^{\text{droplet}} = (-1.1, -0.8, -0.6, -0.2, 0, 0.6, 1.1)$ for the flattest to the most curved surface.

B. Multicomponent concurrent channel flow

In this section, two-dimensional multicomponent fluid flow driven by a volume force is investigated. The geometry of this two-component fluid flow is shown in Fig. 9.

The nonwetting (nw) phase, the phase that is not in direct contact with the solid surface, is considered as a film layer between the wetting (w) phase that covers the surface of the solid in this geometry. The dynamic viscosity ratio is defined as $M = \frac{\mu_{nw}}{\mu_w}$. Given the analytical solution of the Poiseuille flow, the velocity of the fluid in the 2D channel is as follows [38]:

$$\begin{aligned} u(y) &= \tfrac{F_{\text{ext}}}{2\rho_w \nu_w}(b^2 - a^2) + \tfrac{F_{\text{ext}}}{2\rho_{nw}\nu_{nw}}(a^2 - y^2), \quad 0 < |y| < a, \\ u(y) &= \tfrac{F_{\text{ext}}}{2\rho_w \nu_w}(b^2 - y^2), \quad a < |y| < b, \end{aligned} \tag{28}$$

where ν_w and ν_{nw} are kinematic viscosities of the wetting and nonwetting phases, ρ_w and ρ_{nw} are densities of the wetting and nonwetting phases, and F_{ext} is an external volume force.

In this simulation, the fluid current is made by a volumetric force. The solid walls are applied by using the bounce-back boundary condition, and the periodic boundary condition is applied at the sides vertical to the direction of the flow. Also, $G_s = 0$ is set, which results in a 90° contact angle. To be sure about the accuracy of numerical simulations, the effect of the lattice resolution should be analyzed. Therefore, a channel structure with a saturation of 0.44 and a dynamic viscosity ratio of $M = 1$ is considered to investigate the effect of grid size on the accuracy of the computations. The resolution of the domain was changed from 30×30 to 254×254 lattice nodes. Figure 10 shows the variation of normalized average velocity and normalized maximum velocity of the channel

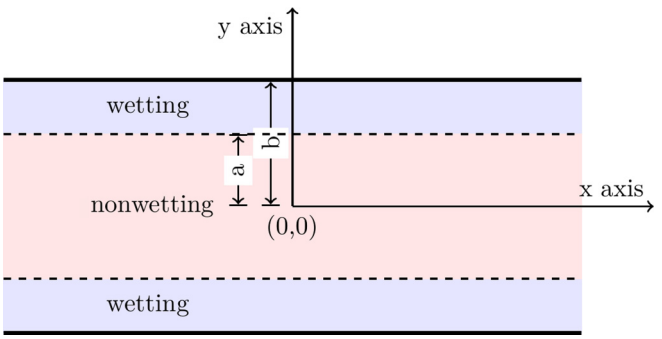

FIG. 9. A view of the geometry of multicomponent fluid flow in the channel.

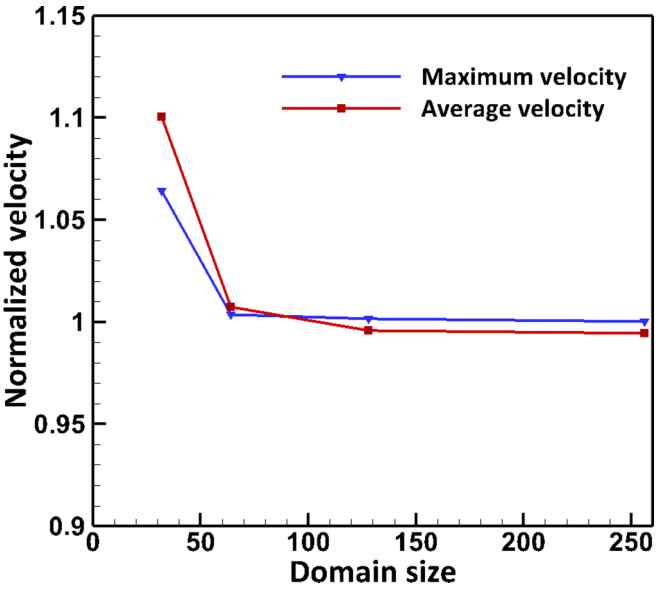

FIG. 10. Normalized average velocity and normalized maximum velocity of the channel flow in terms of grid size.

flow with the number of lattice nodes (mentioned in one direction). In this figure, the results are normalized by the analytical results. As is observed in this figure, the results have good accuracy for lattice nodes of 62×62 and higher domain resolution. For other saturations and viscosity ratios also need approximately the same resolution to be lattice independent. Hence, to have grid-independent results with excellent accuracy, a 126×126 lattice domain is chosen for the present calculations. Figure 11 shows the density profile of the components and the total density of mixture for the channel flow with a dynamic viscosity ratio of $M = 0.0002$, and Fig. 12 shows the contour of the nonwetting fluid's density and the streamlines in the channel.

Due to the fact that there is always some mixing in the immiscible multicomponent fluid flow simulation, in many studies, including Refs. [2,39–41], a distribution for the viscosity

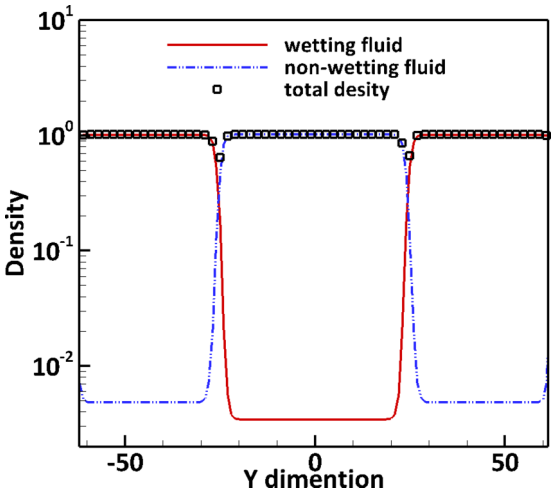

FIG. 11. The density profile of different components in the channel flow for $M = 0.0002$, $a = 25$, and $G = 2.5$.

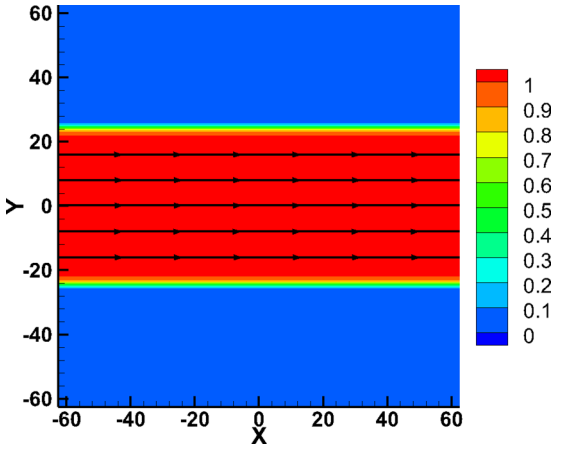

FIG. 12. The density contour and streamlines of nonwetting fluid in the two-component channel flow for $M = 0.0002$, $a = 25$, and $G = 2.5$.

has been used to simulate the two-phase or two-component fluid flow. In this study, according to the Ref. [2], a profile for viscosity is considered based on the mass fraction of the fluids, such that the fluid mixed outside the interface has a viscosity similar to that of the base fluid in which it is mixed. Figures 13 and 14 show the velocity profiles of concurrent channel flow for the dynamic viscosity ratio of 5000 and 0.0002. In these figures, the velocity is normalized by the analytical maximum velocity. In Fig. 13 the maximum velocity is 0.00245, and in Fig. 14 the maximum velocity is 0.00096. In these simulations, the lowest viscosity is set to 0.000167. According to these velocity profiles, it can be seen that the proposed model simulates the immiscible fluid flow for the dynamic viscosity ratio of 5000 and 0.0002 with good accuracy, which is very well consistent with the analytical solution.

In the following, the relative permeability K_r in the two-component channel flow is investigated. The analytical equation of the relative permeability in terms of the wetting phase

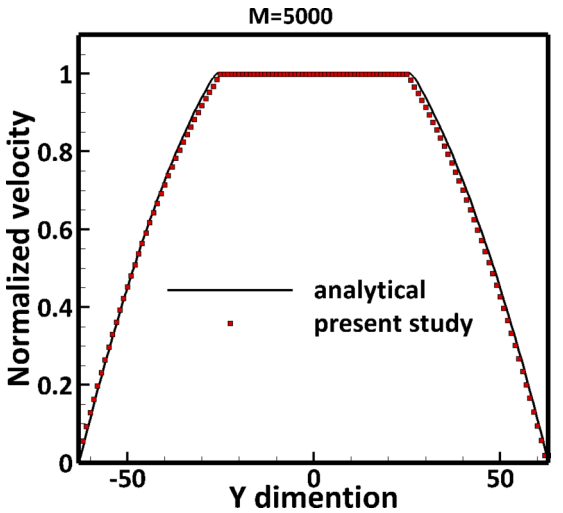

FIG. 13. The velocity profile perpendicular to the flow direction for the channel flow with the dynamic viscosity ratio of $M = 5000$.

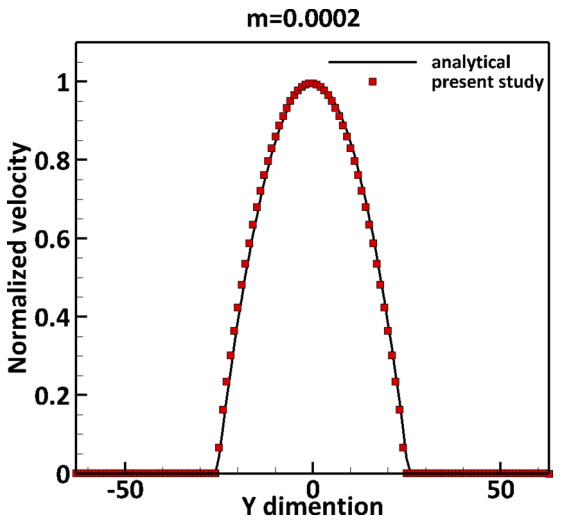

FIG. 14. The velocity profile perpendicular to the flow direction for the channel flow with the dynamic viscosity ratio of $M = 0.0002$.

saturation S_w and nonwetting phase saturation S_{nw} for the two-component Poiseuille flow is as follows [38]:

$$K_{r,w} = \tfrac{1}{2}S_w^2(3 - S_w), \tag{29}$$

$$K_{r,nw} = S_{nw}\left[\frac{3}{2}M + S_{nw}^2\left(1 - \frac{3}{2}M\right)\right]. \tag{30}$$

Figures 15 and 16 show the relative permeability in terms of saturation degree for two wetting and nonwetting fluids with the dynamic viscosity ratios of 0.002 and 0.0002, respectively. As can be seen from these figures, there is good agreement between the relative permeability obtained from the proposed method and that of the analytical solution for two immiscible fluids.

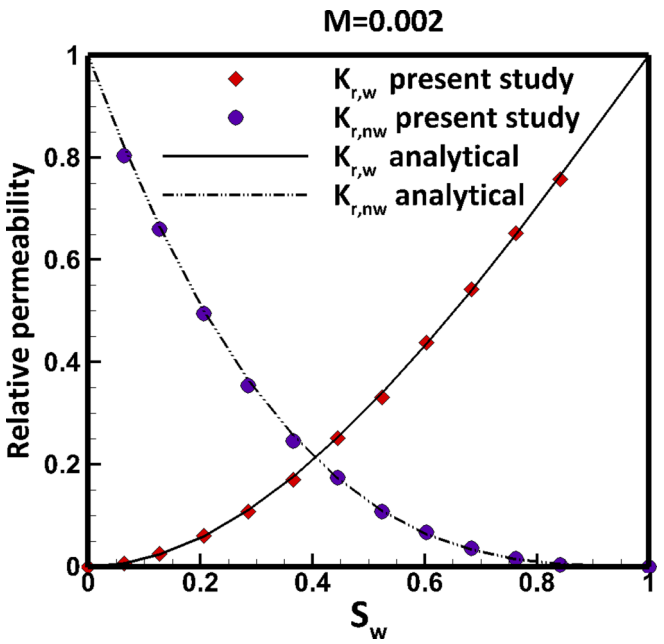

FIG. 15. Relative permeability of wetting and nonwetting fluid for the dynamic viscosity ratio of $M = 0.002$.

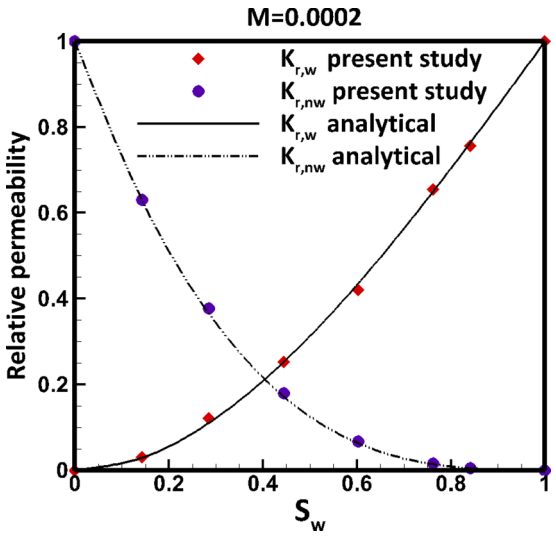

FIG. 16. Relative permeability of wetting and nonwetting fluid for the dynamic viscosity ratio $M = 0.0002$.

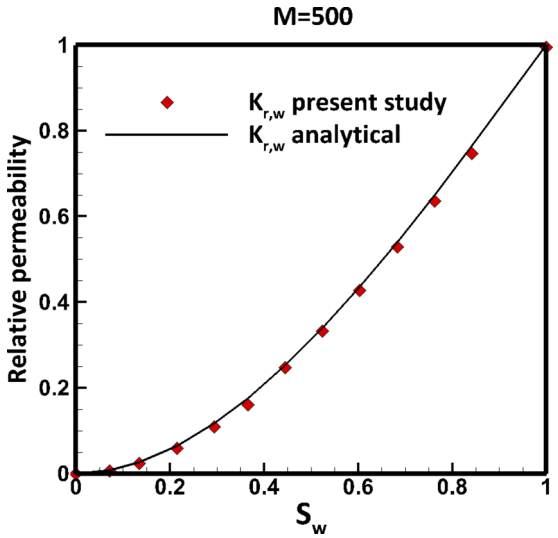

FIG. 18. Relative permeability of wetting fluid in the two-component channel flow for the dynamic viscosity ratio of $M = 500$.

Figures 17 and 18 shows the relative permeability of the nonwetting and wetting fluid for the dynamic viscosity ratio of 500, respectively. Also, Figs. 19 and 20 show the relative permeability of the nonwetting fluid and wetting fluid for the dynamic viscosity ratio of 5000, respectively. It is observed that, in these dynamic viscosity ratios, the wetting relative permeability has a convex curve with values less than one, but the nonwetting relative permeability curve is concave and its values are more than one. As can be seen from these figures, the results have good consistency with the analytical solution, while in the Ref. [1], the results were reported only for dynamic viscosity ratios up to 100. The results show that, when the dynamic viscosity of the wetting fluid is less than that of the nonwetting fluid, the relative permeability of the nonwetting fluid varies greatly and the nonwetting relative permeability curve becomes concave. The relative permeability in some degree of saturation is significantly higher than 1.

C. Coding and computational cost

One of the advantages of the LBM is its high capacity for parallel processing. Notably, the central-moments (CMs) and EDM models are completely compatible with the inherent parallelizability of the LBM. Therefore, the proposed model is coded in parallel in the CUDA-C language. The implementation of the proposed method on GPU is based on Refs. [5,6]. The codes were run on two different machines: a machine equipped by a Tesla-M2050 graphics card with 448 CUDA cores and an AMD CPU 2200 GHz processor and another machine equipped by a GTX-980 graphics card with 2048 CUDA cores and an Intel CPU 3200 GHz processor. Table I shows the performance of implementation for different lattice

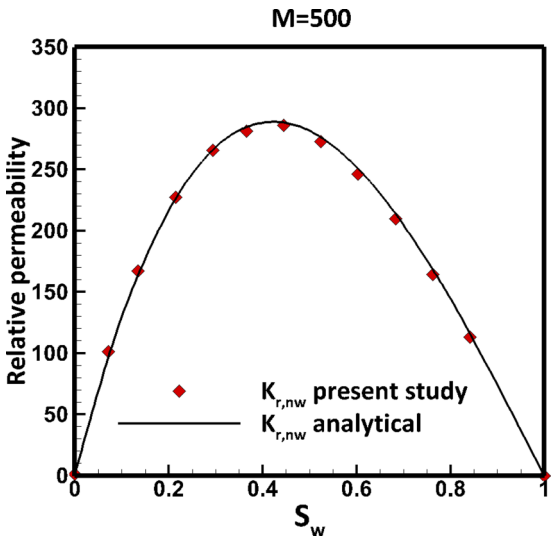

FIG. 17. Relative permeability of nonwetting fluid in the two-component channel flow for the dynamic viscosity ratio of $M = 500$.

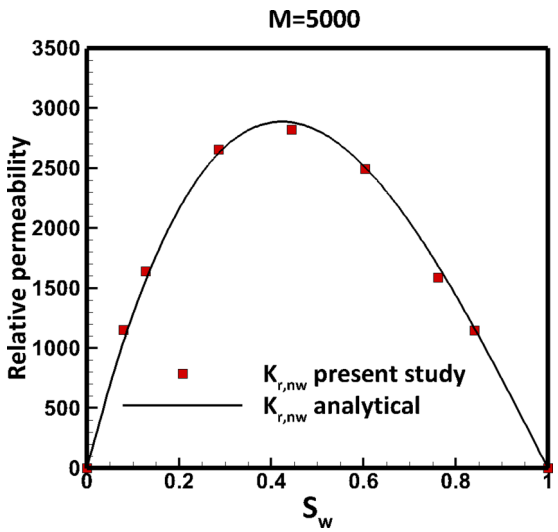

FIG. 19. Relative permeability of nonwetting fluid in the two-component channel flow for the dynamic viscosity ratio of $M = 5000$.

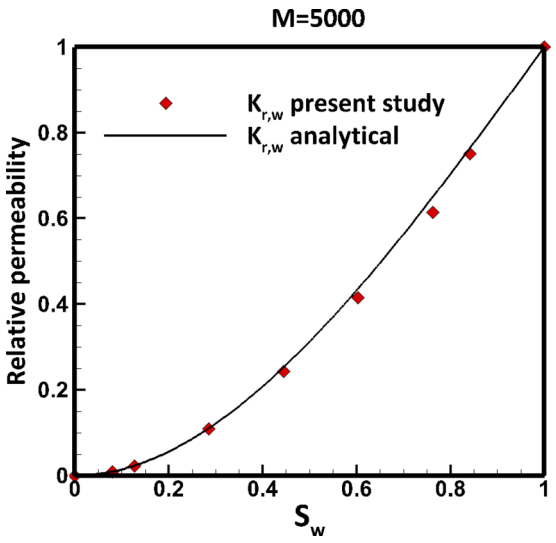

FIG. 20. Relative permeability of wetting fluid in the two-component channel flow for the dynamic viscosity ratio of $M = 5000$.

domains and on different processors in terms of one million lattice site updates per second (MLUPS). According to this table, it can be seen that the proposed model has a high potential for parallelization. Table II shows the duration of 10^5 time steps for the BGK and CMs models. As can be seen, in the presented model, CMs with the isotropy order of 10 (CMs-10th), the duration time is about twice of the BGK model with an isotropy order of 4 (BGK-4th). Although the increase in computation time is undesirable, the proposed model brings great advantages in the stability and flexibility of the multicomponent lattice Boltzmann method. Also, with the high capability of the model for parallel processing, the computation time can be considerably decreased, as shown in Table I.

TABLE I. Performance of implementation in MLUPS (double precision floating point).

Nodes	GPU-GTX980	GPU-TeslaM2050	CPU-Intel74790k
64×64	37.23	12.41	2.56
128×128	39.96	14.37	2.44
256×256	42.55	15.71	1.03
512×512	42.62	15.50	1.04

IV. CONCLUSIONS

In this research, the development of the nonorthogonal central moments model for multicomponent fluid flow simulation by the pseudopotential method is investigated. Based on the nonorthogonal central moments' collision operator, using the capabilities of the EDM force model, and as well as using the multirange model for the intercomponent interaction force, we introduce a robust pseudopotential multicomponent framework for modeling immiscible flows with high viscosity ratios. Numerical computations of the proposed method were done by using a GPU code written in the CUDA-C programming language. The results showed that the CUDA parallel significantly accelerated computation. For example, the comparison of MLUPS between the GTX-980 GPU and one core of the Intel74790k CPU on the 512×512 lattice gives a ratio of $\frac{42.62}{1.04}$, an improvement of about 41 times.

The accuracy of the results of this model was confirmed by using the Laplace law test, simulating a static droplet in the periodic domain, simulating hydrophilic and hydrophobic behavior of the wall surface, studying two-component concurrent flow between two flat plates, and predicting relative permeability in the channel. The results show the good accuracy and high capability of this model. The static droplet is simulated with the dynamic viscosity ratio of 10^5, and the relative permeability is calculated for a dynamic viscosity ratio in the range of 0.002 to 5000 using this method. All results indicate that the proposed model has a high capability for creating a high viscosity ratio in the two-component fluid flow and has high stability for fluid simulation with the viscosity near zero.

TABLE II. Duration time (in seconds) of 10^5 iterations of BGK and CMs models on GPU-GTX980.

Nodes	CMs-10th	BGK-10th	CMs-4th	BGK-4th
64×64	33	23	25	16
128×128	114	76	90	51
256×256	417	261	332	175
512×512	1691	1093	1334	735

APPENDIX

Postcollision distribution functions:

$$f_0^\star = \frac{k_3^\star}{2}\left(-2+u_x^2+u_y^2\right)+\frac{k_4^\star}{2}\left(-u_x^2+u_y^2\right)+4k_5^\star u_x u_y+2k_6^\star u_y+2k_7^\star u_x+k_8^\star + \rho(1-u_x^2-u_y^2+u_x^2u_y^2)+F_0,$$

$$f_1^\star = \frac{k_3^\star}{4}\left(1-u_x-u_x^2-u_y^2\right)+\frac{k_4^\star}{4}\left(1+u_x+u_x^2-u_y^2\right)+k_5^\star(-u_y-2u_xu_y)-k_6^\star u_y + \frac{k_7^\star}{2}(-1-2u_x)-\frac{k_8^\star}{2}+\frac{\rho}{2}\left(u_x+u_x^2-u_xu_y^2-u_x^2u_y^2\right)+F_1,$$

$$f_2^\star = \frac{k_3^\star}{4}\left(1-u_y-u_x^2-u_y^2\right)+\frac{k_4^\star}{4}\left(-1-u_y+u_x^2-u_y^2\right)+k_5^\star(-u_x-2u_xu_y)$$

$$
\begin{aligned}
&+\frac{k_6^\star}{2}(-1-2u_y)-k_7^\star u_x-\frac{k_8^\star}{2}+\frac{\rho}{2}\left(u_y+u_y^2-u_x^2u_y-u_x^2u_y^2\right)+F_2,\\
f_3^\star=&\frac{k_3^\star}{4}\left(1+u_x-u_x^2-u_y^2\right)+\frac{k_4^\star}{4}\left(1-u_x+u_x^2-u_y^2\right)+k_5^\star(u_y-2u_xu_y)-k_6^\star u_y\\
&+\frac{k_7^\star}{2}\left(1-2u_x\right)-\frac{k_8^\star}{2}+\frac{\rho}{2}\left(-u_x+u_x^2+u_xu_y^2-u_x^2u_y^2\right)+F_3,\\
f_4^\star=&\frac{k_3^\star}{4}\left(1+u_y-u_x^2-u_y^2\right)+\frac{k_4^\star}{4}\left(-1+u_y+u_x^2-u_y^2\right)+k_5^\star\left(u_x-2u_xu_y\right)\\
&+\frac{k_6^\star}{2}(1-2u_y)-k_7^\star u_x-\frac{k_8^\star}{2}+\frac{\rho}{2}\left(-u_y+u_y^2+u_x^2u_y-u_x^2u_y^2\right)+F_4,\\
f_5^\star=&\frac{k_3^\star}{8}\left(u_x+u_y+u_x^2+u_y^2\right)+\frac{k_4^\star}{8}\left(-u_x+u_y-u_x^2+u_y^2\right)+\frac{k_5^\star}{4}(1+2u_x+2u_y+4u_xu_y)\\
&+\frac{k_6^\star}{4}(1+2u_y)+\frac{k_7^\star}{4}(1+2u_x)+\frac{k_8^\star}{4}+\frac{\rho}{4}\left(u_xu_y+u_x^2u_y+u_xu_y^2+u_x^2u_y^2\right)+F_5,\\
f_6^\star=&\frac{k_3^\star}{8}\left(-u_x+u_y+u_x^2+u_y^2\right)+\frac{k_4^\star}{8}\left(u_x+u_y-u_x^2+u_y^2\right)+\frac{k_5^\star}{4}(-1+2u_x-2u_y+4u_xu_y)\\
&+\frac{k_6^\star}{4}(1+2u_y)+\frac{k_7^\star}{4}(-1+2u_x)+\frac{k_8^\star}{4}+\frac{\rho}{4}\left(-u_xu_y+u_x^2u_y-u_xu_y^2+u_x^2u_y^2\right)+F_6,\\
f_7^\star=&\frac{k_3^\star}{8}\left(-u_x-u_y+u_x^2+u_y^2\right)+\frac{k_4^\star}{8}\left(u_x-u_y-u_x^2+u_y^2\right)+\frac{k_5^\star}{4}(1-2u_x-2u_y+4u_xu_y)\\
&+\frac{k_6^\star}{4}(-1+2u_y)+\frac{k_7^\star}{4}(-1+2u_x)+\frac{k_8^\star}{4}+\frac{\rho}{4}\left(u_xu_y-u_x^2u_y-u_xu_y^2+u_x^2u_y^2\right)\\
&+F_7,\\
f_8^\star=&\frac{k_3^\star}{8}\left(u_x-u_y+u_x^2+u_y^2\right)+\frac{k_4^\star}{8}\left(-u_x-u_y-u_x^2+u_y^2\right)+\frac{k_5^\star}{4}(-1-2u_x+2u_y+4u_xu_y)\\
&+\frac{k_6^\star}{4}(-1+2u_y)+\frac{k_7^\star}{4}(1+2u_x)+\frac{k_8^\star}{4}+\frac{\rho}{4}\left(-u_xu_y-u_x^2u_y+u_xu_y^2+u_x^2u_y^2\right)+F_8.
\end{aligned}
\tag{A1}
$$

[1] M. L. Porter, E. T. Coon, Q. Kang, J. D. Moulton, and J. W. Carey, Multicomponent interparticle-potential lattice Boltzmann model for fluids with large viscosity ratios, Phys. Rev. E **86**, 036701 (2012).

[2] H. Otomo, B. Crouse, M. Dressler, D. M. Freed, I. Staroselsky, R. Zhang, and H. Chen, Multi-component lattice Boltzmann models for accurate simulation of flows with wide viscosity variation, Comput. Fluids **172**, 674 (2018).

[3] S. Chen, H. Chen, D. Martinez, and W. Matthaeus, Lattice Boltzmann Model for Simulation of Magnetohydrodynamics, Phys. Rev. Lett. **67**, 3776 (1991).

[4] S. Chen and G. D. Doolen, Lattice Boltzmann method for fluid flows, Annu. Rev. Fluid Mech. **30**, 329 (1998).

[5] J. Tölke, Implementation of a lattice Boltzmann kernel using the compute unified device architecture developed by nvidia, Comput. Visualization Sci. **13**, 29 (2008).

[6] F. Kuznik, C. Obrecht, G. Rusaouen, and J.-J. Roux, LBM based flow simulation using GPU computing processor, Comput. Math. Appl. **59**, 2380 (2010).

[7] F. Gharibi, S. Jafari, M. Rahnama, B. Khalili, and E. J. Javaran, Simulation of flow in granular porous media using combined lattice Boltzmann method and smoothed profile method, Comput. Fluids **177**, 1 (2018).

[8] X. Shan, Multicomponent lattice Boltzmann model from continuum kinetic theory, Phys. Rev. E **81**, 045701(R) (2010).

[9] D. Qian, J. B. McLaughlin, K. Sankaranarayanan, S. Sundaresan, and K. Kontomaris, Simulation of bubble breakup dynamics in homogeneous turbulence, Chem. Eng. Commun. **193**, 1038 (2006).

[10] N. S. Martys, J. G. Hagedorn, D. Goujon, and J. E. Devaney, Large-scale simulations of single- and multicomponent flow in porous media, in *Developments in X-Ray Tomography II*, edited by U. Bonse (SPIE, 1999), Vol. 3772, pp. 205–213.

[11] A. Ghassemi and A. Pak, Numerical study of factors influencing relative permeabilities of two immiscible fluids flowing through porous media using lattice Boltzmann method, J. Pet. Sci. Eng **77**, 135 (2011).

[12] H. Zhao, Z. Ning, Q. Kang, L. Chen, and T. Zhao, Relative permeability of two immiscible fluids flowing through porous media determined by lattice Boltzmann method, Int. Commun. Heat Mass Transfer **85**, 53 (2017).

[13] D. Zhang, S. Li, S. Jiao, Y. Shang, and M. Dong, Relative permeability of three immiscible fluids in random porous media determined by the lattice Boltzmann method, Int. J. Heat Mass Transfer **134**, 311 (2019).

[14] S. Frijters, F. Günther, and J. Harting, Effects of nanoparticles and surfactant on droplets in shear flow, Soft Matter **8**, 6542 (2012).

[15] Y. Chen, Q. Kang, Q. Cai, M. Wang, and D. Zhang, Lattice Boltzmann simulation of particle motion in binary immiscible fluids, Commun. Comput. Phys. **18**, 757 (2015).

[16] X. Shan, Analysis and reduction of the spurious current in a class of multiphase lattice Boltzmann models, Phys. Rev. E **73**, 047701 (2006).

[17] M. Sbragaglia, R. Benzi, L. Biferale, S. Succi, K. Sugiyama, and F. Toschi, Generalized lattice Boltzmann method with multirange pseudopotential, Phys. Rev. E **75**, 026702 (2007).

[18] G. Falcucci, S. Ubertinib, and S. Succic, Lattice Boltzmann simulations of phase separating flows at large density ratios the case of doubly attractive pseudo potentials, Soft Matter **6**, 4357 (2010).

[19] Q. Kang, D. Zhang, and S. Chen, Immiscible displacement in a channel: Simulations of fingering in two dimensions, Adv. Water Resour. **27**, 13 (2004).

[20] L. Chen, Q. Kang, Y. Mu, Y.-L. He, and W.-Q. Tao, A critical review of the pseudopotential multiphase lattice Boltzmann model: Methods and applications, Int. J. Heat Mass Transfer **76**, 210 (2014).

[21] J. Yang and E. S. Boek, A comparison study of multi-component lattice Boltzmann models for flow in porous media applications, Comput. Math. Appl. **65**, 882 (2013).

[22] P. Berghout and H. E. V. den Akker, Simulating drop formation at an aperture by means of a multi-component pseudo-potential lattice Boltzmann model, Int. J. Heat Fluid Flow **75**, 153 (2019).

[23] X. Shan and H. Chen, Lattice Boltzmann model for simulating flows with multiple phases and components, Phys. Rev. E **47**, 1815 (1993).

[24] A. Hu, L. Li, and R. Uddin, Force method in a pseudo-potential lattice Boltzmann model, J. Comput. Phys. **294**, 78 (2015).

[25] A. Kupershtokh, D. Medvedev, and D. Karpov, On equations of state in a lattice Boltzmann method, Comput. Math. Appl. **58**, 965 (2009).

[26] Q. Li, K. H. Luo, and X. J. Li, Forcing scheme in pseudopotential lattice Boltzmann model for multiphase flows, Phys. Rev. E **86**, 016709 (2012).

[27] Z. Guo, C. Zheng, and B. Shi, Discrete lattice effects on the forcing term in the lattice Boltzmann method, Phys. Rev. E **65**, 046308 (2002).

[28] M. Geier, A. Greiner, and J. G. Korvink, Cascaded digital lattice Boltzmann automata for high Reynolds number flow, Phys. Rev. E **73**, 066705 (2006).

[29] A. D. Rosis, Non-orthogonal central moments relaxing to a discrete equilibrium: A D2Q9 lattice Boltzmann model, Europhys. Lett. **116**, 44003 (2016).

[30] G. R. McNamara and G. Zanetti, Use of the Boltzmann Equation to Simulate Lattice Gas Automata, Phys. Rev. Lett. **61**, 2332 (1988).

[31] H. Chen, S. Chen, and W. H. Matthaeus, Recovery of the Navier-Stokes equations using a lattice-gas Boltzmann method, Phys. Rev. A **45**, R5339 (1992).

[32] T. Krüger, H. Kusumaatmaja, A. Kuzmin, O. Shardt, G. Silva, and E. M. Viggen, *The Lattice Boltzmann Method: Principles and Practice* (Springer International Publishing, Cham, 2017).

[33] S. Schmieschek and J. Harting, Contact angle determination in multicomponent lattice Boltzmann simulations, Commun. Comput. Phys. **9**, 1165 (2011).

[34] H. Otomo, H. Fan, Y. Li, M. Dressler, I. Staroselsky, R. Zhang, and H. Chen, Studies of accurate multi-component lattice Boltzmann models on benchmark cases required for engineering applications, J. Comput. Sci. **17**, 334 (2016).

[35] X. Shan and H. Chen, Simulation of nonideal gases and liquid-gas phase transitions by the lattice Boltzmann equation, Phys. Rev. E **49**, 2941 (1994).

[36] D. T. MC Sukop, *Lattice Boltzmann Modeling, An Introduction for Geoscientists and Engineers* (Springer, Berlin Heidelberg, 2006).

[37] B. Dong, Y. Y. Yan, and W. Z. Li, LBM simulation of viscous fingering phenomenon in immiscible displacement of two fluids in porous media, Transp. Porous Media **88**, 293 (2011).

[38] A. G. Yiotis, J. Psihogios, M. E. Kainourgiakis, A. Papaioannou, and A. K. Stubos, A lattice Boltzmann study of viscous coupling effects in immiscible two-phase flow in porous media, Colloids Surf., A **300**, 35 (2007).

[39] A. Fakhari, T. Mitchell, C. Leonardi, and D. Bolster, Improved locality of the phase-field lattice-Boltzmann model for immiscible fluids at high density ratios, Phys. Rev. E **96**, 053301 (2017).

[40] W.-Z. Fang, L. Chen, Q.-J. Kang, and W.-Q. Tao, Lattice Boltzmann modeling of pool boiling with large liquid-gas density ratio, Int. J. Therm. Sci. **114**, 172 (2017).

[41] H. Chen, J. Zhang, Y. Zhang, and Z. Wei, Simulation on a gravity-driven dripping of droplet into micro-channels using the lattice Boltzmann method, Int. J. Heat Mass Transfer **126**, 61 (2018).